Building and Environment 244 (2023) 110814

Contents lists available at ScienceDirect

Building and Environment

journal homepage: www.elsevier.com/locate/buildenv

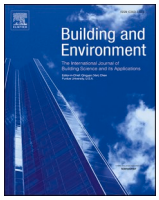

Evaluation of frost prevention strategies for membrane energy exchangers

Hongyu Bai [a], Peng Liu [b,*], Hans Martin Mathisen [a]

[a] Department of Energy and Process Engineering, Norwegian University of Science and Technology, 7491, Trondheim, Norway
[b] Department of Architecture, Materials and Structures, SINTEF Community, 7465, Trondheim, Norway

ARTICLE INFO

Keywords:
Membrane energy exchanger
Frost prevention
Quasi-counter-flow
Mechanical ventilation
Cold climate

ABSTRACT

In cold climates, the application of heat recovery is restricted by the issue of frost, which causes potential damage to heat exchangers and degrades their effectiveness. Membrane energy exchangers (MEEs), which enable simultaneous heat and moisture transfer, can reduce and delay frost formation and accumulation in cold climates. MEEs are recognized as the essential component for the new generation of Heating, Ventilation, and Air Conditioning (HVAC) systems. Despite of extensive studies on heat and mass transfer characterising and increased use of MEEs, the evaluation of suitable frost control strategies for the emerging MEEs in cold climates are still missing. This study presents numerical models of a quasi-counter-flow membrane energy exchanger (QCFMEE) and a quasi-counter-flow heat exchanger (QCFHE). Three different frost prevention strategies are examined: preheating outdoor air, heating room air and bypassing outdoor air. These strategies' threshold values to prevent frost are calculated numerically and validated against experimental measurements. The results show that QCFMEE has lower threshold values and thus better frost tolerance ability compared with QCFHE because of mass transfer through the membranes. Moreover, the frost prevention strategies are evaluated based on annual energy consumption, energy saving ratio (ESR), and complexity of control for real-life applications. The simulated results show that among the discussed frost prevention strategies, preheating outdoor air has the advantage of the lowest energy consumption and highest ESR. Meanwhile, heating room air consumes the most energy and faces the problem of overheating outdoor air. Finally, concerning the bypassing outdoor air strategy, the significant fluctuation of its threshold values increases the complexity of control for real-life applications.

1. Introduction

Energy consumed by heating, ventilation and air-conditioning (HVAC) systems is responsible for 40–60% of total energy consumption in the building sector [1], and it is increasing with occupants' growing requirements for comfort [2]. Recovering waste heat is one energy-efficient process that can be applied to reduce buildings' energy consumption [2]. Membrane energy exchangers (MEEs) have been increasingly used to recover both sensible and latent heat in exhaust air from indoor environments in order to treat outdoor air; such exchangers are a key component of next-generation HVAC systems [3,4]. Several literature reviews on MEEs have been carried out, focusing on fundamentals and engineering applications [4], membrane material properties [5], the structures and operating conditions of MEEs [6], and MEEs' applications in cold climates [7]. In MEEs, exhaust air and supply air channels are separated by membranes, and heat and moisture recovery are driven by the temperature and humidity difference between supply air and exhaust air [3]. In areas with cold climates such as Russia, Canada and Scandinavia, exhaust air heat loss accounts for a significant part of the total heat loss from buildings [8]. By recovering heat and moisture from indoor air, MEEs would not only reduce heating energy consumption but also improve the indoor comfort level, as they have the potential to add humidity to dry indoor air in cold regions [7]. A recently published study [9] analyzed the impact of moisture recovery with effectiveness from 0 to 90% on different room types in a single-family house in Norway. The results showed that the optimal moisture recovery effectiveness for a satisfactory and healthy indoor moisture level can be determined by assessing the time fraction of relative humidity (RH) levels within the defined RH ranges. The membranes used are also assumed to be completely impermeable to airborne pollutants and odours; As a result, they are exhausted to the outdoors without being transferred to the supply air side [10]. Fig. 1 illustrates the mechanism of heat and mass transfer through a membrane in winter [10].

In cold climates, the application of heat recovery is restricted by the issue of frost, which can deteriorate the performance of heat exchangers in several ways: reduced heat recovery effectiveness, increased fan power consumption and even serious deformation or damage due to

* Corresponding author.
E-mail address: peng.liu@sintef.no (P. Liu).

https://doi.org/10.1016/j.buildenv.2023.110814
Received 23 June 2023; Received in revised form 18 August 2023; Accepted 6 September 2023
Available online 7 September 2023

Nomenclature

c_p	specific heat capacity (J/kg K)
d_a	thickness of air channels (m)
d_i	side length of the air flow inlet (m)
d_o	parameter to determine the length of pure counter part (m)
D	diffusivity (m^2 /s)
D_H	hydraulic diameter (m)
E	energy consumption (J)
$E_{bypassed}$	bypassed ratio
h	convective heat transfer coefficient (W/m^2K)
j	Colburn factor
k	convective mass transfer coefficient (m/s)
Le	Lewis number
$\dot{m}$	mass flow rate (kg/s)
Nu	Nusselt number
Pe	Peclet number
Pr	Prandtl number
Q	power (W)
Re	Reynolds number
Sc	Schmidt number
Sh	Sherwood number
T	temperature ($^{\circ}C$)
U	overall heat transfer coefficient (W/m^2 K)
U_m	overall mass transfer coefficient (kg/m^2 s)
u	velocity component in x direction (m/s)
V	velocity (m/s)
$\dot{V}$	volume flow rate (m^3 /h)
v	velocity component in y direction (m/s)
v_a	kinetic viscosity of air (m^2/s)
W	humidity ratio (kg/kg dry air)

Greeks

δ	thickness (m)
ε	effectiveness
λ	thermal conductivity (W/mK)
ρ	density (kg/m^3)
τ	time (second)
ψ	stream function

Subscripts

a	air
counter	counter flow
cr	critical
cross	cross flow
e	exhaust air side
ei	exhaust air inlet
eo	exhaust air outlet
in	inlet
lat	latent
max	maximum
mem	membrane
o	outdoor
o ut	outlet
r	room
s	supply air side
sen	sensible
si	supply air inlet
so	supply air outlet
tot	total

Abbreviations

CFD	computational fluid dynamics
ESR	energy saving ratio
HVAC	heating, ventilation, and air-conditioning
IAQ	indoor air quality
QCFHE	quasi-counter-flow heat exchanger
QCFMEE	quasi-counter-flow membrane energy exchanger
RH	relative humidity (%)

long-term frost accumulation [11,12]. Frost occurs in heat exchangers if, at some point, the temperature of a heat transfer surface is lower than the freezing point and also lower than the dew point temperature of the airflow in contact with the surface [11]. A comprehensive review of frost problems in air-to-air heat/energy exchangers is given in Ref. [13]. Frost normally occurs in the exhaust air side of heat exchangers, as exhaust air from indoor spaces has a higher moisture content. In MEEs, the dew point of exhaust air is much lower than in a sensible-only heat exchanger, as both temperature and humidity are reduced during the heat-recovery process. This gives MEEs an advantage over sensible-only heat exchangers: they tolerate a much lower supply air temperature [14]. Niroomand et al. [15] experimentally investigated frost on a semipermeable membrane and an impermeable surface under different vapour transfer rates. They found that the transfer of water vapour through the membrane slows the process of frost formation, and water droplets remain in the liquid phase on semipermeable membranes for a

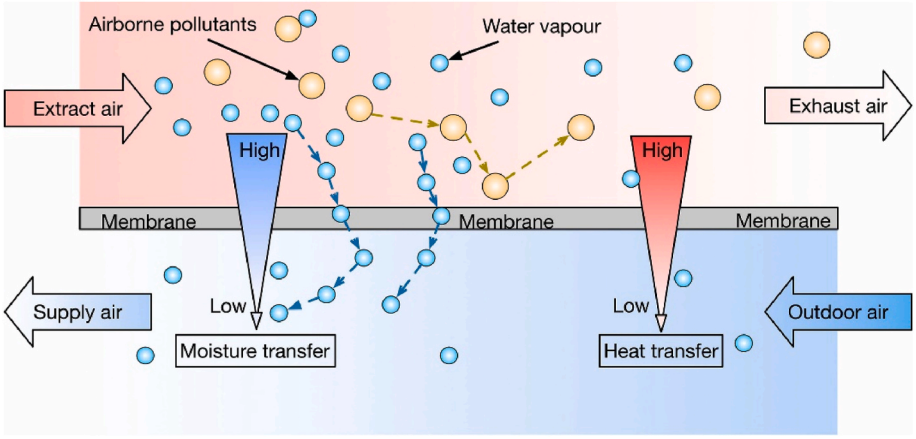

Fig. 1. Mechanism of heat and mass transfer through a membrane in winter [10].

long time. Although using membranes with better vapour permeability could delay frost onset, Navid et al. [16] pointed out that increasing the moisture transfer ability of membranes by a factor of two would only achieve a delay of less than 5 min. Therefore, in practice, delaying frost is not as promising as avoiding the saturation of moist air by simultaneously drying and cooling the air.

In order to avoid the negative impacts of frost inside heat exchangers, frost control strategies must be integrated with mechanical ventilation systems. Frost control includes both frost prevention and defrosting; while the former strategy prevents the occurrence of frost in the first place, the latter regularly removes frost build-up [17]. In a literature review, Bai et al. [7] found that frost prevention has several advantages over defrosting, including simple operation, uninterrupted ventilation, and better indoor air quality (IAQ). Various frost prevention strategies were also summarized: preheating outdoor air, heating room air, bypassing outdoor air, and reducing the exchanger's effectiveness. Liu et al. [18] studied the energy-saving potential of a heat-recovery system using MEE with the strategy of preheating outdoor air. Their results showed that less energy was used for preheating MEE than for a plate heat exchanger in which only sensible heat was recovered. Compared with other frost control strategies, preheating outdoor air can significantly reduce operating cost, even though the upfront cost is relatively high [19]. Nourozi et al. [20] presented a ventilation system that uses wastewater to preheat outdoor air to reduce the need for defrosting in Sweden. The threshold values of frost used in their simulation are constant values. Nasr et al. [21] experimentally evaluated the performance of a cross-flow sensible-only heat exchanger in cold climates using two frost control methods: preheating outdoor air and periodically bypassing outdoor air. They concluded that preheating outdoor air performed best regarding energy saving percentage, which was two times higher than when using bypass outdoor air. Similar results can be found in Ref. [22], in which the authors claimed that for a counter-flow plate heat exchanger, preheating outdoor air is more energy-efficient than bypassing outdoor air under sub-zero operating conditions.

Despite the increasing use of membrane energy exchangers in ventilation systems for cold climates, frost control strategies to sustain their safe operation and high energy recovery efficiency are underexplored. Frost onset prediction and control are particularly imperative considering that the membrane materials are typically thin and vulnerable to frost. Moreover, the mass transfer characteristics may be sensitive to changes in operating conditions such as condensation or frost, which in turn influence the MEEs' performance. The main novelty and contributions of this study are as follows:

1. This study numerically investigated frost thresholds for a quasi-counter-flow membrane energy exchanger (QCFMEE) and a quasi-counter-flow heat exchanger (QCFHE). The developed models were validated against experimental measurements. Unlike experimental studies on specific heat exchangers, the numerical models in this study can be generalized to exchangers of different sizes.
2. Three commonly used frost control approaches for QCFMEE and QCFHE were compared for different cold climates. Thresholds were developed and used to evaluate performance indicators including energy consumption during the heating season, energy saving ratio (ESR), and complexity of control for real-life applications. The findings can support the design and standardization of membrane energy exchangers for use in cold climates.
3. The numerical models developed in this work require little computational effort compared to simulations using computational fluid dynamics (CFD). As a result, the models can be feasibly used for global sensitivity analysis or the optimization of frost thresholds and the performance of membrane energy exchangers, which may not be possible to realize with CFD due to its computational demands.

2. Numerical models of QCFMEE and QCFHE

2.1. Assumptions

Assumptions made for the simplification of this study's numerical modelling include the following:

1) The exchanger is well insulated; thus, the heat and mass transfer between the exchanger and the environment are not considered.
2) Axial conduction in air flows is neglected, as Peclet numbers (P_e) in air flows are much larger than 20 [23].
3) Air flows are considered laminar, as Reynolds numbers (R_e) are lower than 2300 in all cases.
4) The heat released during condensation is neglected, as it has a limited impact on the membrane surface temperature and frost in the exchanger when the indoor RH is lower than 30% [24].
5) Air flows are assumed to be 2-dimensional, incompressible and Newtonian fluid with constant thermal properties.
6) The air temperature, humidity and velocity are uniform at the inlets of both the supply and exhaust air channels of the exchanger.

2.2. Velocity fields simulation

To solve the temperature and humidity fields for the air flows, velocity fields are solved first. One supply air channel, one exhaust air channel and the membrane layer between these adjacent air channels are selected for simulation. The coordinate system of QCFMEE for the simulation is selected and illustrated in Fig. 2(a). The geometric parameters of QCMEE are illustrated in Fig. 2(b).

For 2-dimensional and incompressible ideal flows, the 3-dimensional Navior–Stokes equations can be simplified to stream functions with boundary conditions. For viscous flows, stream functions can also be applied to obtain the velocity distribution of the flows through thin channels at low Re numbers [25]. The stream function ψ is given as follows:

$$\nabla^2\psi = \frac{\partial^2\psi}{\partial x^2} + \frac{\partial^2\psi}{\partial y^2} = 0 \tag{1}$$

For any location in the velocity fields, the velocity components in the x and y directions are as follows:

$$u = \frac{\partial\psi}{\partial y} \tag{2}$$

$$v = -\frac{\partial\psi}{\partial x} \tag{3}$$

where u and v are the velocity components in the x and y directions, respectively (m/s).

The above stream function ψ automatically satisfies the continuity equation:

$$\frac{\partial u}{\partial x} + \frac{\partial v}{\partial y} = \frac{\partial^2\psi}{\partial x\partial y} - \frac{\partial^2\psi}{\partial x\partial y} = 0 \tag{4}$$

Based on Eq. (1), the stream function is transferred to a second-order Laplace equation that satisfies the boundary conditions.

2.3. Heat and mass transfer governing equations

2.3.1. Heat transfer governing equations

On the supply air side,

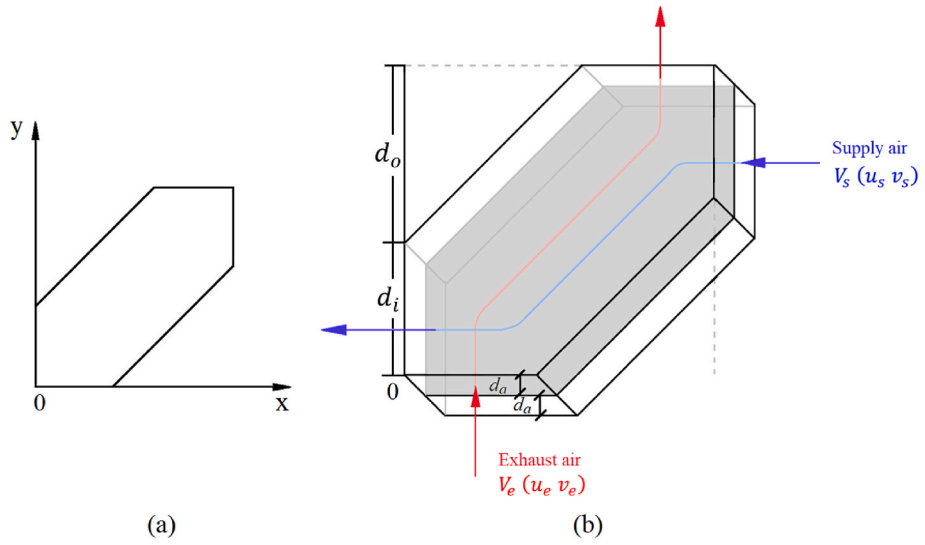

Fig. 2. (a) Coordinate system used for the numerical simulation of QCFMEE (b)geometric parameters of QCFMEE.

$$Q_{out} - Q_{in} = d_a dy \rho_a c_{p,a} \left(u_s \frac{\partial T_s}{\partial x} + T_s \frac{\partial u_s}{\partial x} \right) dx + d_a dx \rho_a c_{p,a} \left(v_s \frac{\partial T_s}{\partial y} + T_s \frac{\partial v_s}{\partial y} \right) dy$$
$$= d_a dx dy \rho_a c_{p,a} \left(u_s \frac{\partial T_s}{\partial x} + v_s \frac{\partial T_s}{\partial y} + T_s \left(\frac{\partial u_s}{\partial x} + \frac{\partial v_s}{\partial y} \right) \right) \tag{5}$$

Based on the continuity equation

$$\frac{\partial u_s}{\partial x} + \frac{\partial v_s}{\partial y} = 0 \tag{6}$$

substituting Eq. (6) to Eq. (5) gives the following:

$$Q_{out} - Q_{in} = d_a dx dy \rho_a c_{p,a} \left(u_s \frac{\partial T_s}{\partial x} + v_s \frac{\partial T_s}{\partial y} \right) \tag{7}$$

where Q_{out} and Q_{in} are heat flows out from and into the control volume (W); d_a is the thickness of each air channel shown in Fig. (2) (m); ρ_a is the density of air (kg/m^3); $c_{p,a}$ is the specific heat capacity of air (J/kg K); and T_s is the temperature of supply air flow ($^\circ C$).

Based on the conservation of energy,

$$Q_{out} - Q_{in} = U(T_e - T_s) dx dy \tag{8}$$

where T_e is the temperature of exhaust air flow ($^\circ C$) and U is the overall heat transfer coefficient (W/m^2 K). The latter can be obtained by

$$U = \left(\frac{1}{h_s} + \frac{\delta_{mem}}{\lambda_{mem}} + \frac{1}{h_e} \right)^{-1} \tag{9}$$

where h_s and h_e are convective heat transfer coefficients for supply air and exhaust air, respectively (W/m^2 K); δ_{mem} is the thickness of the membrane layer (m); and λ_{mem} is the thermal conductivity of the membrane layer (W/m K).

Therefore, the heat transfer governing equation on the supply air side is as follows:

$$d_a \rho_a c_{p,a} \left(u_s \frac{\partial T_s}{\partial x} + v_s \frac{\partial T_s}{\partial y} \right) = U(T_e - T_s) \tag{10}$$

Applying the same method, the heat transfer governing equation on the exhaust air side is the following:

$$d_a \rho_a c_{p,a} \left(u_e \frac{\partial T_e}{\partial x} + v_e \frac{\partial T_e}{\partial y} \right) = -U(T_e - T_s) \tag{11}$$

2.3.2. Mass transfer governing equations

On the supply air side,

$$\dot{M}_{out} - \dot{M}_{in} = d_a dy \rho_a \left(u_s \frac{\partial W_s}{\partial x} + W_s \frac{\partial u_s}{\partial x} \right) dx + d_a dx \rho_a \left(v_s \frac{\partial W_s}{\partial y} + W_s \frac{\partial v_s}{\partial y} \right) dy$$
$$= d_a dx dy \rho_a \left(u_s \frac{\partial W_s}{\partial x} + v_s \frac{\partial W_s}{\partial y} \right) \tag{12}$$

where $\dot{M}_{out}$ and $\dot{M}_{in}$ are mass flows out from and into the control volume (kg/s) and W_s is the humidity ratio of supply air (kg/kg dry air).

Based on the conservation of mass,

$$\dot{M}_{out} - \dot{M}_{in} = U_m (W_e - W_s) dx dy \tag{13}$$

where W_e is the humidity ratio of exhaust air (kg/kg dry air) and U_m is the overall mass transfer coefficient (kg/m^2 s). The latter can be obtained by the following:

$$U_m = \left(\frac{1}{k_s \rho_a} + \frac{\delta_{mem}}{D_{mem} \rho_a} + \frac{1}{k_e \rho_a} \right)^{-1} \tag{14}$$

where k_s and k_e are the convective mass transfer coefficients for supply air and exhaust air, respectively (m/s) and D_{mem} is the diffusivity of the membrane layer (m^2/s).

Thus, the mass transfer governing equation on the supply air side is as follows:

$$d_a \rho_a \left(u_s \frac{\partial W_s}{\partial x} + v_s \frac{\partial W_s}{\partial y} \right) = U_m (W_e - W_s) \tag{15}$$

Applying the same method, the mass transfer governing equation on the exhaust air side is the following:

$$d_a \rho_a \left(u_e \frac{\partial W_e}{\partial x} + v_e \frac{\partial W_e}{\partial y} \right) = -U_m (W_e - W_s) \tag{16}$$

In Eqs. (9) and (14), h_s, h_e, k_s and k_e are required for the solution of the governing equations. The methods used to obtain these parameters are given in Appendix A, and the procedures to solve the governing equations are explained in Appendix B.

2.4. Performance evaluation

After obtaining the temperature and humidity distributions in the exchanger, its performance can be evaluated by calculating the sensible

effectiveness ε_{sen} and latent effectiveness ε_{lat}, which are defined as follows:

$$\varepsilon_{sen} = \frac{Q}{Q_{max}} = \frac{T_{ei} - T_{eo}}{T_{ei} - T_{si}} \tag{17}$$

$$\varepsilon_{lat} = \frac{\dot{M}}{\dot{M}_{max}} = \frac{W_{ei} - W_{eo}}{W_{ei} - W_{si}} \tag{18}$$

where Q is the heat transfer rate on the exhaust air or supply air side (W); Q_{max} is the maximum potential heat transfer rate inthe heat exchanger (W); $\dot{M}$ is the mass transfer rate on the exhaust air or supply air side (kg/s); $\dot{M}_{max}$ is the maximum potential mass transfer rate in the enthalpy exchanger (kg/s); T_{si} and T_{ei} are supply and exhaust air temperatures at the inlets of QCFMEE, respectively (°C); W_{si} and W_{ei} are supply and exhaust air humidity ratios at the inlets of QCFMEE, respectively (kg/kg dry air); and T_{eo} and W_{eo} are the average outlet temperature (°C) and humidity ratio (kg/kg dry air) on the exhaust air side.

3. Different frost prevention strategies and their threshold values

3.1. Frost limits

Prior to demonstrating the three types of frost prevention strategies discussed in later sections, it is important to introduce the concept of frost limits.

The condition under which frost starts forming in heat exchangers is called the frost limit [26]. This study uses the frost limits explained by Liu et al. [27,28], who indicated that the frost limits include the critical outdoor temperature T_{cr} (°C) and condensation limit. Frost was considered to occur when the membrane temperature on the exhaust air side is below the freezing point and the exhaust air adjacent to the membrane is condensing, meaning that the RH of the exhaust air adjacent to the membrane reaches 100%. The lowest temperature of outdoor air that would maintain the membrane surface temperature above the freezing point is defined as the critical outdoor temperature T_{cr}. When the outdoor temperature is below T_{cr}, the lowest RH of room air that would prevent it from condensing is defined as the condensation limit. Thus, frost limits are expressed as combinations of outdoor temperature T_o and room air relative humidity RH_r.

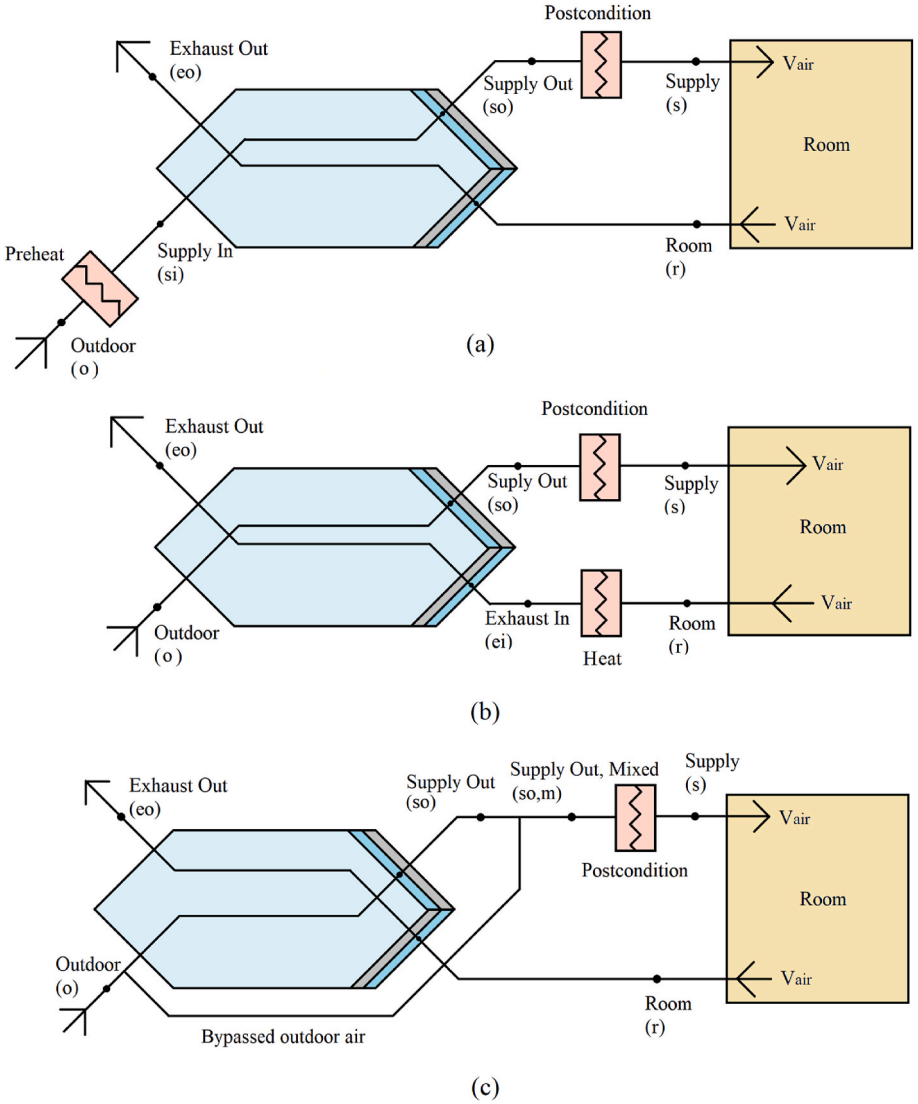

Fig. 3. Schematics of different frost prevention strategies: (a) preheating outdoor air, (b) heating room air and (c) bypassing outdoor air.

3.2. Frost prevention strategies

In this paper, three types of frost prevention strategies are discussed: preheating outdoor air, heating room air, and bypassing outdoor air. The strategies are illustrated in Fig. 3.

For all the frost prevention strategies, frost limits are applied first to determine whether these strategies are triggered. When the frost is predicted to occur, for the preheating outdoor air strategy, cold outdoor air is heated by the preheater from T_o to the threshold temperature, which is denoted as T_{si} in Fig. 3 (a). After exiting the exchanger, this airstream is post-conditioned in another heater, where it is heated to the supply air temperature T_s. In this paper, the outdoor air RH (RH_o) is assumed to be a constant 80%, and the room temperature T_r is assumed to be a constant 21 $^\circ C$. Then, T_s is then set to be 2 $^\circ C$ lower than T_r to avoid draught [29], which is 19 $^\circ C$. For the heating room air strategy, when frost is predicted, the room air is heated in the heater from T_r to the threshold temperature, which is denoted as T_{ei} in Fig. 3 (b). In the exchanger, the temperature of the outdoor air increases from T_o to T_{so}. This airstream is then post-conditioned before being supplied to the room. It should be emphasised that T_{so} could be lower or higher than the pre-set T_s; therefore, the postcondition could be sensible heating or cooling. For bypassing outdoor air, when frost is predicted, a certain amount of outdoor air is bypassed without entering the exchanger, as illustrated in Fig. 3 (c). A ratio called the bypassed ratio is defined as follows:

$$E_{bypassed} = \frac{\dot{V}_{a,bypassed}}{\dot{V}_a} \tag{19}$$

where $\dot{V}_{a,bypassed}$ is the air flow rate of the bypassed outdoor airstream (m^3/h) and $\dot{V}_a$ is the air flow rate of the outdoor airstream (m^3/h).

The remaining outdoor air enters the exchanger normally, and these two airstreams join at the exit of the exchanger. This mixed airstream is post-conditioned in a sensible heater, where its temperature increases from $T_{so,m}$ to T_s.

In conclusion, threshold values have various meanings for different frost prevention strategies. For the preheating outdoor air strategy, the threshold value is T_{si}; for the heating room air strategy, the threshold value is T_{ei}; and for the bypassing outdoor air strategy, the threshold value is $E_{bypassed}$.

3.3. Energy consumption analysis

For energy consumption analysis, only energy consumed for air treatment is considered in this study. In particular, fan power and other energy consumption are not considered. For the preheating outdoor air strategy, the energy used for preheating (J) is as follows:

$$E_{preheat} = \dot{m}_a c_{p,a}(T_{si} - T_o)\Delta\tau \tag{20}$$

where $\dot{m}_a$ is the mass flow rate of supply air or exhaust air in each channel (kg/s) and Δt is a specific time span used for energy consumption calculation (s).

The energy used for postconditioning (J) is as follows:

$$E_{postcondition} = \dot{m}_a c_{p,a}(T_s - T_{so})\Delta\tau \tag{21}$$

For the heating room air strategy specifically, the energy used for heating (J) is

$$E_{heat} = \dot{m}_a c_{p,a}(T_{ei} - T_r)\Delta\tau \tag{22}$$

For the bypassing outdoor air strategy specifically, the energy used for postconditioning (J) is

$$E_{postcondition} = \dot{m}_a c_{p,a}\left(T_s - T_{so,m}\right)\Delta\tau \tag{23}$$

Then, the total energy used for ventilation with heat recovery and frost prevention (J) is as follows:

$$E_{tot,HR} = \sum\left(E_{preheat}, E_{heat}, E_{postcondition}\right) \tag{24}$$

ESR is defined to investigate the energy saving potential of applying heat recovery with frost prevention strategies as compared with energy consumption without using heat recovery. It is defined as follows:

$$ESR = \frac{E_{tot} - E_{tot,HR}}{E_{tot}} \tag{25}$$

where E_{tot} is the total energy used for ventilation without heat recovery (J):

$$E_{tot} = \dot{m}_a c_{p,a}(T_s - T_o)\Delta\tau \tag{26}$$

4. Experimental test

4.1. QCFMEE structure and experimental test facility

The QCFMEE used in the experimental test consists of nine layers of air passages, which are composed of plastic frames, sealing brackets and membranes. Air passages are also supported by corrugated aluminium spacers, which enhance heat and mass transfer by interrupting the boundary layers. The polypropylene membranes used to separate air passages are hydrophobic, porous membranes that can transfer moisture but are impermeable to odours and other pollutants [4]. Fig. 4 shows the structure of a QCFMEE.

A test rig was developed to test the sensible and latent effectiveness of a QCFMEE. Fig. 5 provides a schematic view of the test rig. As shown in Fig. 5, the test rig consists of an MEE, inlet expansion diffusor, outlet contraction diffusor, fans, air ducts, and measurement instrumentation. Supply air with a low temperature was generated in the environmental chamber, while exhaust air with a fixed temperature of 21 $^\circ C$ was introduced from the ambient air in the laboratory. Four fans were utilized to maintain balanced air flow rates on the supply air and exhaust air sides.

T-type thermocouples were made by the laboratory and calibrated from -20 $^\circ C$ to 20 $^\circ C$ using the t-type thermocouple made by Pettersen™, which has an accuracy of $\pm$ 0.05$^\circ C$. The thermocouples were mounted at the inlets and outlets of the supply air and exhaust air sides. For each port, four thermocouples were evenly distributed at the horizontal centreline of the inlet or outlet. Air RH was measured using Vaisala™ humidity and temperature transmitters (HMT330). Air flow rates in supply air and exhaust air sides were measured by orifice plates. Air straighters were placed in front of the orifice plates to shorten the length of the ducts and reduce the ductwork heat loss. All the measured parameters were acquired using the NI™ data acquisition system, which was read by LabView™ every 30 s.

4.2. Uncertainty analysis

In this study, the uncertainty analysis of Coleman et al. [31] is applied using a 95% confidence interval. The general uncertainty is given as follows:

$$U_r = \sqrt{\left[\left(\frac{\partial r}{\partial X_1}U_{X_1}\right)^2 + \left(\frac{\partial r}{\partial X_2}U_{X_2}\right)^2 + \ldots + \left(\frac{\partial r}{\partial X_J}U_{X_J}\right)^2\right]} \tag{27}$$

The uncertainty U consists of bias error B and precision error P:

$$U = \sqrt{B^2 + P^2} \tag{28}$$

Bias error is mainly from calibration, data acquisition and data reduction. Precision error is determined by:

$$P = tS \tag{29}$$

where t is calculated as 2.021 when the number of readings for one measured parameter is 41 [31].

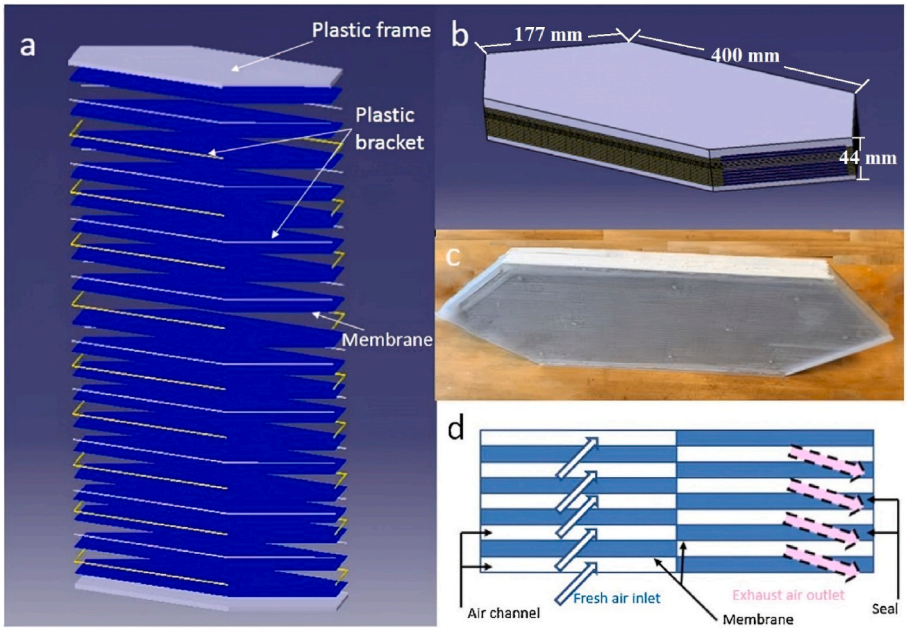

Fig. 4. Structure of a QCFMEE, including (a) 3D explosion schematic view of a QCFMEE (b) 3D view of a QCFMEE (c) photograph of a QCFMEE used in the experimental test and (d) supply air inlet and exhaust air outlet of a QFMEE [28,30].

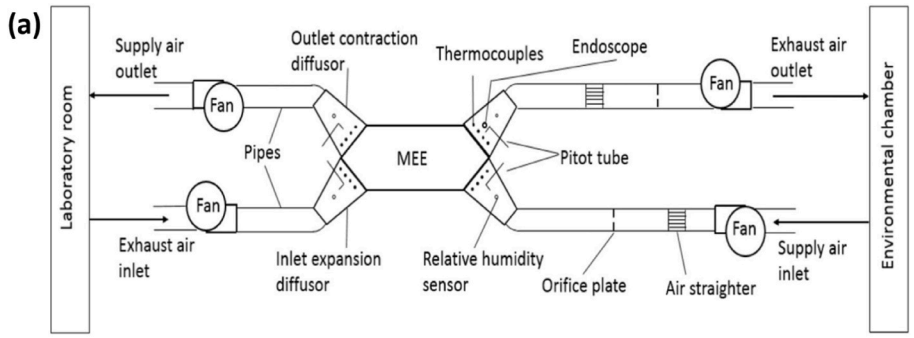

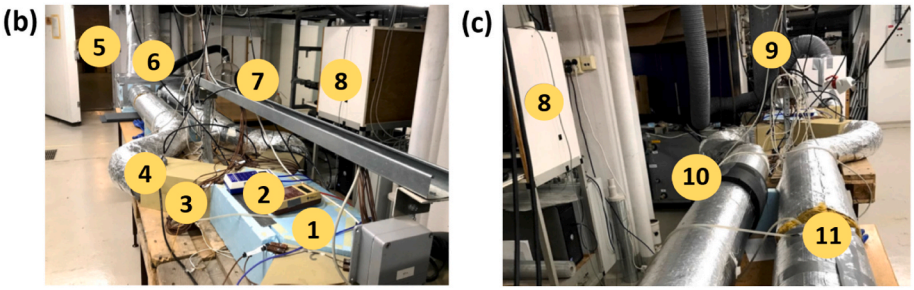

Fig. 5. (a) The schematic view of the test rig for a QCFMEE [27,28], (b) and (c) pictures of the test rig including membrane energy exchanger. Numbers correspond to different components of the MEE test rig, where: 1 - MEE core; 2 - Micro-manometers; 3 - Thermocouples; 4 – Relative humidity sensor; 5 - Environmental chamber; 6 - Ventilation channel connections; 7 – Instrument wires connecting to data acquisition system; 8 - Computer with LabVIEW; 9 – Extract air ductwork to the basement exhaust; 10 - Air straightener; 11 -Orifice plate with tubes connecting to a manometer (adapted from Ref. [10]).

Table 1
Uncertainties of the main measured and calculated parameters.

Air temperature	±0.16°*C* at 11.4 °*C*	Air volume flow rate	±1.57% at 25.2 m^3/h
RH at 23 °*C*	±1.3% at 40.0%	Sensible effectiveness	±3.2% at 92.5%
Pressure drop	±5.6 Pa at 524.1Pa	Latent effectiveness	±5.8% at 78.2%

Table 1 shows the uncertainties of the main tested parameters and calculated results.

4.3. Validation of QCFMEE effectiveness

The numerical simulation of the sensible and latent effectiveness of QCFMEE is validated by both the numerical solution explained by Kays and London [32] and the experimental results under three air flow rates: 15.12 m^3/h, 21.24 m^3/h and 24.84 m^3/h. Kays and London [32] divided

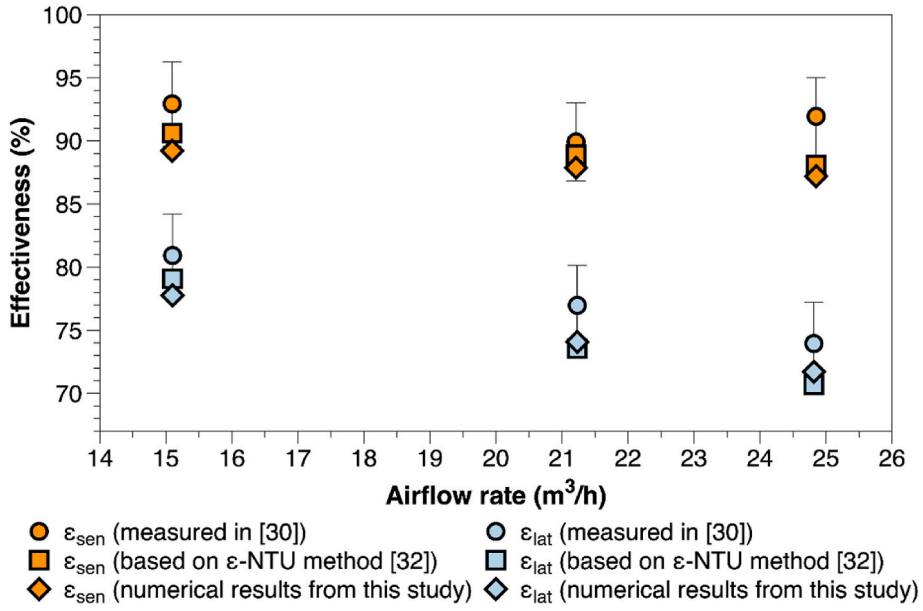

Fig. 6. Comparison among numerical, Kays and London [32], and experimental results of ε_{sen}.

the quasi-counter-flow exchanger in the cross-flow section and counter-flow section. Numerical procedures were applied for the cross-flow and counter-flow sections separately. Effectiveness can be obtained as a function of the heat capacity ratio *Cr*, number of transfer units in the cross-flow section NTU_{cross} and number of transfer units in counter-flow section $NTU_{counter}$. Comparisons among numerical, Kays and London, and experimental results for sensible and latent effectiveness of ACFMEE are plotted in Fig. 6. For both sensible and latent effectiveness, simulation results are lower than the experimental results. This is because in the experiment presented in literature [30], the QCFMEE used for testing have aluminium spacer placed onto the supply and exhaust air channel to support the membrane. The corrugated mesh spacers can enhance the heat and mass transfer in the QCFMEE due to the enhanced convection by the local turbulence. In this study air channels are assumed to be open channels, which results in relatively lower effectiveness. Another possible reason why the calculated effectiveness is lower than the experimental results is that the entrance effect, which increase the heat transfer coefficient are not considered in both Kay's method and this numerical study. In general, good agreements between the numerical simulation results and both the Kays and London solutions and the test results are observed. The maximum discrepancy between the numerical simulation results and the Kays and London results is 1.15%, while the maximum discrepancy between the numerical simulation results and experimental results is 3.6%.

5. Results and discussion

5.1. Frost locations inside the exchanger

Investigating the locations of frost formation inside the exchanger

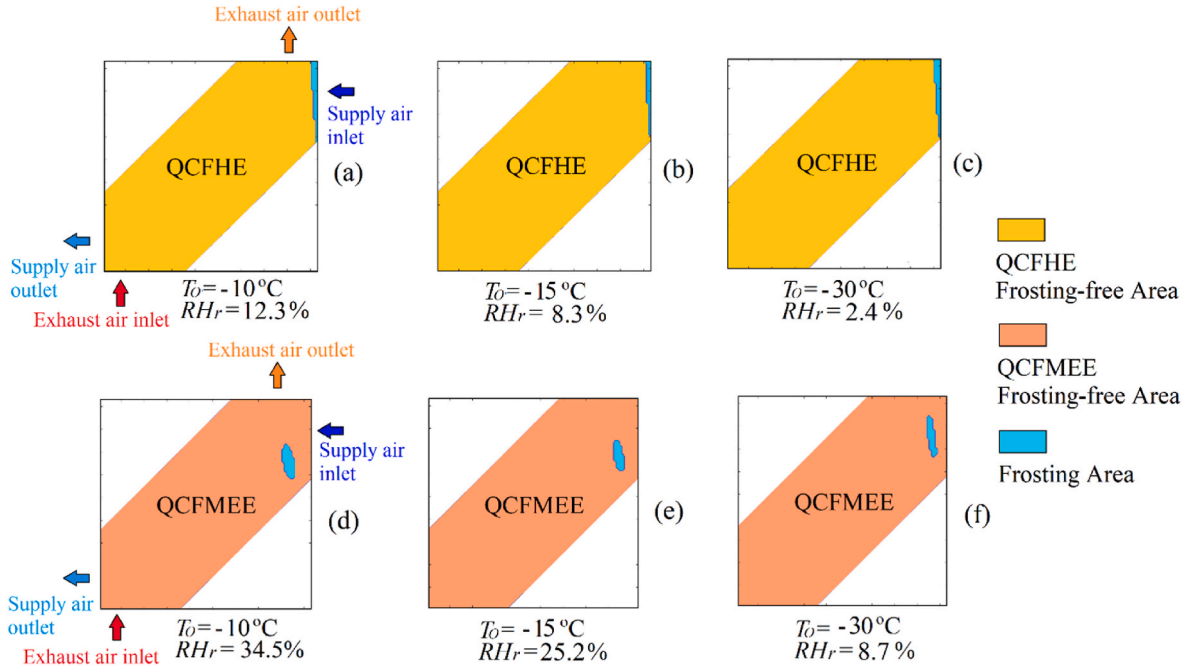

Fig. 7. Locations where frost first occurs in QCFHE and QCFMEE under various conditions.

can provide a better understanding of frost development and guide future research on defrosting methods. In the previous literature on QCFHE, frost is assumed to first form at the exhaust air outlet closest to the supply air inlet, which was defined as the 'cold corner' [27,28]. This is easy to understand; as there is no mass transfer in the QCFHE, the 'cold corner' has both the lowest temperature and highest RH. Frost limits were then developed based on the air temperature and RH at the 'cold corner' of the QCFHE. However, RH is determined by both air temperature and humidity ratio. As a result, while the temperature and humidity ratio of exhaust air at the 'cold corner' of the QCFMEE are indeed the lowest for the entire temperature and humidity ratio distributions across the exchanger, its RH is not necessarily the highest. Thus, saturated conditions (when RH reaches 100%) could first occur in an inner location of the QCFMEE, which is not necessarily the 'cold corner'. The frost onset location is related to both temperature and humidity ratio distributions that are determined by the operating conditions, heat and moisture transfer characteristics of the exchanger. Fig. 7 illustrates the locations where frost first occurs in QCFHE and QCFMEE and their corresponding conditions. In this figure, RH_o and T_r are kept constant as 80% and 22 °C respectively. It can be seen from Fig. 7 that frost first occurs from the 'cold corner' in QCFHE. In contrast, the frost first builds from the inside in QCFMEE rather than the 'cold corner' under all conditions. These are the locations that have the highest RH. Moreover, compared with QCFHE, QCFMEE has better frost tolerance. For example, when the outdoor air temperature $T_o = -10\,^{\circ}C$, frost is first found in QCFHE when the RH_r is 12.3%. By contrast, frost first occurs in QCFMEE when RH_r is 34.5%. The same difference trend can also be found under $T_o = -15\,^{\circ}C$ and $-30\,^{\circ}C$.

This trend can also be found in Fig. 8, where frosting areas are pictured in QCFHE and QCFMEE under two operating conditions. The operating conditions of RH_o and T_r remained 80% and 22 °C. Under each operating condition, the frosting area in QCFMEE is building from the inside of the exchanger, and the frosting area size is significantly smaller than it in QCFHE. The results showed in Fig. 8 confirmed the reduced frost risk in membrane energy exchangers resulting from the reduced dew point in exhaust air due to its moisture transfer feature compared to the sensible-only heat exchanger. Thus, it can be beneficial to use MEEs in cold climate to mitigate frost risk and energy used for frost control. However, considering the durability of the thin membranes in MEEs, proper frost control to ensure frost-free operation in MEEs are more critical as the membrane may be more vulnerable to the accumulated frost compared to the metallic or plastic heat exchangers.

5.2. Threshold values for different frost prevention strategies

Fig. 9 illustrates the threshold values for the preheating outdoor air strategy for both QCFMEE and QCFHE. Fig. 9 (a) shows the relationship between RH_r and threshold T_{si} under three different air flow rates: 72, 144 and 216 m^3/h. To investigate the influence of RH_r, T_o is kept at a constant value of $-10\,^{\circ}C$. Fig. 9 (b) shows the relationship between T_o and threshold T_{si} under the same air flow rates. In this case, RH_r is kept at a constant value of 40% to examine the influence of T_o.

It is found that the threshold T_{si} increases with both RH_r and T_o, meaning that higher values of RH_r or T_o would require preheating T_o to a higher T_{si}. First, the influence of RH_r on T_{si} under the same T_o is analyzed. Assume a specific combination of RH_r and T_{si} for which the highest RH on the exhaust air side is 100%. Then, increase RH_r to a higher level of $RH_r^{'}$; the humidity difference between the supply and exhaust air sides also increases. As a result, if T_o is still heated to the original T_{si}, the highest RH in the exhaust air side would exceed 100%. Therefore, T_o must be heated to a higher temperature $T_{si}^{'}$ to ensure that the highest RH in the exhaust air side reaches 100%. Similar analyses can be applied to study the influence of T_o on T_{si} under the same RH_r. Under a specific combination of T_o and T_{si} for which the highest RH in the exhaust air side is 100%, increase T_o to a higher temperature of $T_o^{'}$. Because the RH_o is assumed to be constant, increasing T_o would also increase the humidity ratio of outdoor air, which would reduce the humidity difference between the supply and exhaust air sides. Subsequently, the highest RH in the exhaust air side would exceed 100% if T_o is still heated to the original T_{si}, meaning that T_o needs to be heated to a higher temperature $T_{si}^{'}$ to ensure that the highest RH in the exhaust air side reaches 100%.

Compared with QCFHE, QCFMEE has much a lower threshold T_{si} and thus better tolerance for frost formation. For example, under $\dot{V}_a = 216$ m^3/h and $RH_r = 30\%$, T_o must be heated from $-10\,^{\circ}C$ to $-8\,^{\circ}C$ in QCFMEE to avoid frost. By contrast, it must be heated to $0\,^{\circ}C$ in QCFHE.

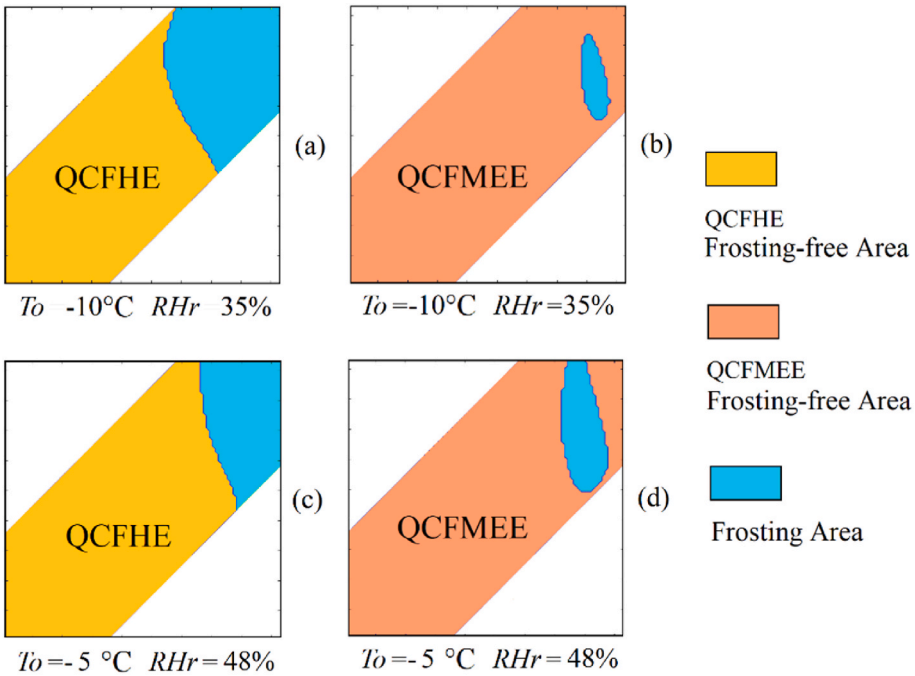

Fig. 8. Locations of frost in QCFHE and QCFMEE under various conditions.

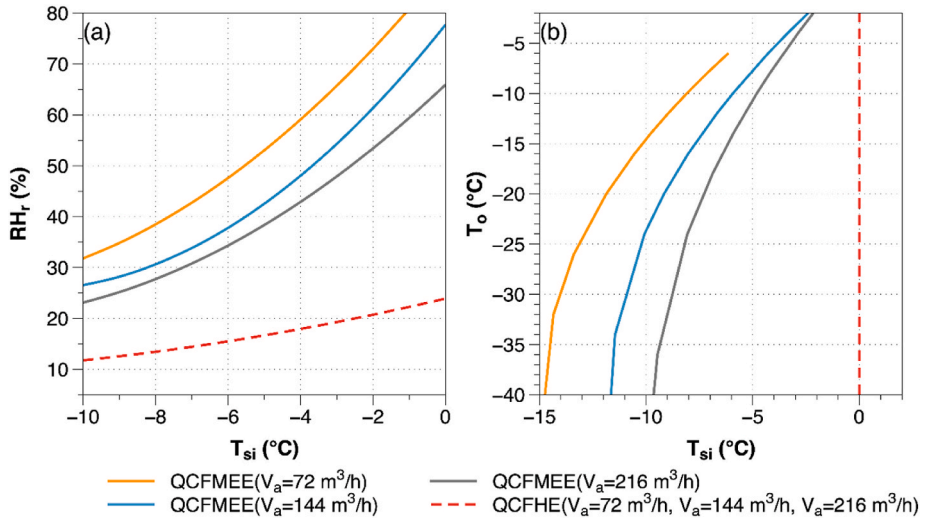

Fig. 9. Threshold values for the preheating outdoor air strategy, including (a) RH_r against T_{si} at $T_o = -10°C$ (b) T_o against T_{si} at $RH_r = 40\%$.

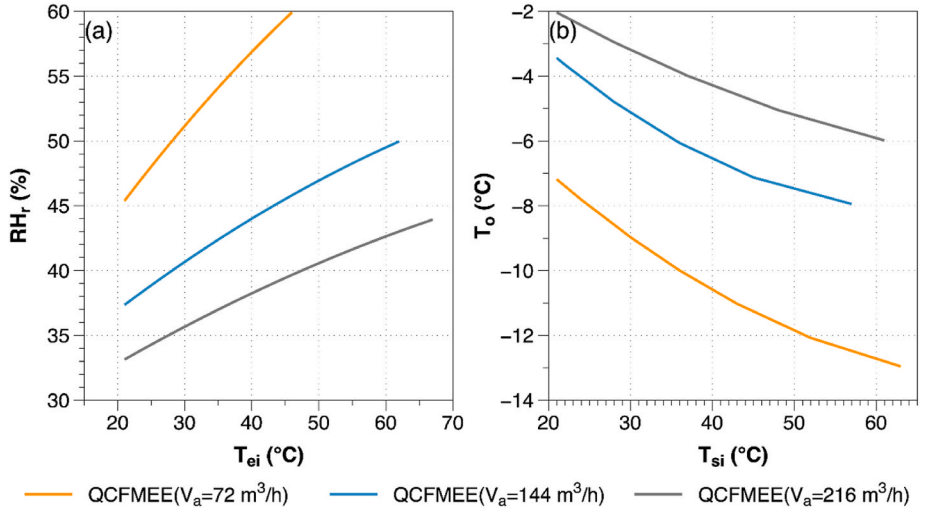

Fig. 10. Threshold values for the heating room air strategy, including (a) RH_r against T_{ei} at $T_o = -10°C$ (b) T_o against T_{ei} at $RH_r = 40\%$.

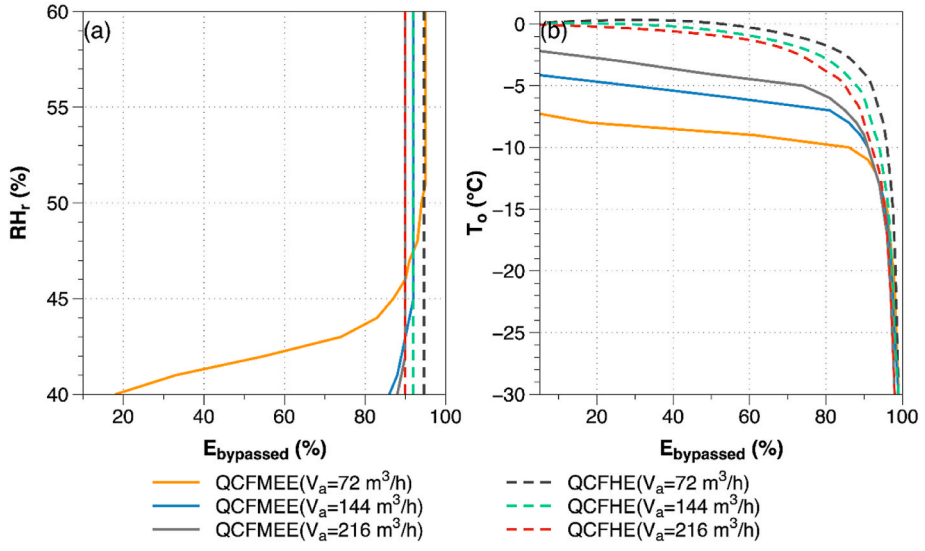

Fig. 11. Threshold values for the bypassing outdoor air strategy (a) RH_r against $E_{bypassed}$ at $T_o = -10°C$ (b) T_o against $E_{bypassed}$ at $RH_r = 40\%$.

This is attributed to better mass transfer ability, or higher latent effectiveness, in QCFMEE than in QCFHE.

Air flow rate has a negligent impact on threshold T_{si} in QCFHE, while its impact on threshold T_{si} in QCFMEE is significant. For QCFMEE, both sensible and latent effectiveness will be affected when changing $\dot{V}_a$. Reducing $\dot{V}_a$ will enhance both sensible and latent effectiveness, and the combined effect is a lower RH on the exhaust air side. As a result, the threshold value is improved by reducing the $\dot{V}_a$ for the preheating outdoor air strategy. This means that T_o can be heated to a lower T_{si} under a low $\dot{V}_a$.

Fig. 10 illustrates the threshold values for the heating room air strategy for the QCFMEE. Under each $\dot{V}_a$, the threshold T_{ei} is related to RH_r and T_o. The impact of RH_r on the threshold value is the same as in the preheating outdoor air strategy: a higher RH_r would cause room air to be heated to a higher T_{ei}. However, the threshold T_{ei} would decrease with T_o. This is because the highest RH in the exhaust air side would decrease with T_o, meaning that the room air can be heated to a lower temperature $T_{ei}^{'}$. $\dot{V}_a$ has a considerable effect on the threshold T_{ei}, which can be significantly improved by reducing $\dot{V}_a$. Fig. 10 demonstrates that room air must be heated to a rather high temperature in order to prevent frost formation under some conditions. For a QCFHE, the required threshold temperature is even higher, which can be difficult to achieve in reality; this is the reason why the threshold values for a QCFHE are not plotted in Fig. 10. High T_{ei} could also cause the problem of overheating the outdoor air in the exchanger. This will be discussed in more detail in Section 5.3.

Fig. 11 illustrates the threshold values for the bypassing outdoor air strategy for the QCFMEE and QCFHE. For both CFMEE and QCFHE, the threshold $E_{bypassed}$ is influenced by RH_r and T_o. In order to investigate the effects of RH_r and T_o on $E_{bypassed}$, it is important to first explore the effects of changing $E_{bypassed}$ on the heat exchanger. For any enthalpy exchanger, ε_s and ε_l have already been defined by Eqs. (17) and (18). By applying the $\varepsilon - NTU$ method, ε_s and ε_l can be expressed as follows:

$$\varepsilon_s = f(NTU, Cr) = f\left(\frac{UA}{\dot{m}_{amin}c_{p,a}}, \frac{\dot{m}_{amax}c_{p,a}}{\dot{m}_{amin}c_{p,a}}\right) \tag{30}$$

$$\varepsilon_l = f(NTU_m, Cr) = f\left(\frac{U_m A}{\dot{m}_{amin}}, \frac{\dot{m}_{amax}c_{p,a}}{\dot{m}_{amin}c_{p,a}}\right) \tag{31}$$

where NTU and NTU_m are the number of heat transfer units and the number of mass transfer units, respectively; A is the total heat transfer area (m^2); Cr is the heat capacity ratio; $\dot{m}_{amax}$ is the maximum air mass flow rate (kg/s; whichever is higher of $\dot{m}_a$ on the exhaust air side or supply air side); $\dot{m}_{amin}$ is the minimum air mass flow rate (kg/s; whichever is lower of $\dot{m}_a$ on the exhaust air side or supply air side). ε_s is positively related to both NTU and Cr, and ε_l is positively related to both NTU_m and Cr. Regarding heat transfer, reducing $E_{bypassed}$ would decrease $\dot{m}_{amin}$ in the exchanger; thus, both NTU and Cr would increase. As a result, ε_s is enhanced in the exchanger. However, reducing $\dot{m}_{amin}$ would decrease the exchanger's maximum potential heat transfer rate, which would lead to a reduction in the heat transfer rate in the exhaust air side. T_{eo} would increase given that the air mass flow rate on the exhaust air side remains unchanged. Similar analyses can be applied to the mass transfer, and it can be concluded that W_{eo} would increase as well. The combined effect is that the maximum RH on the exhaust air side would decrease when reducing $E_{bypassed}$. In other words, reducing $E_{bypassed}$ would benefit the exchanger by improving frost tolerance. As a consequence, given a specific $E_{bypassed}$ for which the highest RH in the exhaust air side is 100%, a higher RH_r and a lower T_o would cause it to exceed 100%, and a lower $E_{bypassed}^{'}$ would be required to prevent frost.

Regarding $\dot{V}_a$, it has a different influence on the threshold $E_{bypassed}$ for QCFMEE and QCFHE. For QCFHE, a reduced $\dot{V}_a$ would deteriorate the frost tolerance ability by increasing the ε_s; thus, a lower $E_{bypassed}$ is needed to prevent frost formation. For QCFMEE, both ε_s and ε_l would be enhanced by reducing $\dot{V}_a$, and their combined effect is a better frost tolerance ability, which leads to a higher $E_{bypassed}$.

5.3. Comparison among different frost prevention strategies

The preheating outdoor air strategy is examined first. Fig. 12 shows monthly accumulated results for the energy consumption and ESR for the cities of Montreal and Oslo during the heating season. The period between December and March is selected as the heating season. Montreal and Oslo are selected as case cities, as they represent the warm-summer humid continental climate (Dfb) and oceanic climate (Cfb) according to the Köppen climate classification [33]. The annual heating degree days (HDD) for Montreal in 2022 is 4117 (18 °C as the base temperature) [34] while it is 2823 for Oslo [35].

During the heating season, the average outdoor temperature in Oslo is lower than in Montreal. As a result, $E_{preheat}$, $E_{postcondition}$ and $E_{tot,HR}$ in Oslo are lower than those in Montreal for each month. In particular, the $E_{tot,HR}$ in Oslo for the heating season is 2240 MJ, which is 54% lower than $E_{tot,HR}$ in Montreal for the heating season. For both cities, $E_{preheat}$ has a close relationship with outdoor air temperature, and a low outdoor temperature leads to a high $E_{preheat}$. For example, the highest values of $E_{preheat}$ in Montreal and Oslo occur in the coldest month (January), with energy consumption of 998 MJ and 470 MJ, respectively. By contrast, $E_{postcondition}$ has no obvious relationship with outdoor air temperature. For both cities, ESR is significantly impacted by $E_{tot,HR}$, and a low $E_{tot,HR}$ results in a high ESR.

In the simulation, the threshold values discussed in Section 5.2 are used for the preheating outdoor air strategy; this means that for each outdoor air condition, there is a corresponding threshold T_{si}. The Norwegian Technical Specification SN-NSPEK 3031:2021 [36] also demonstrates a frost prevention method, which is to preheat the outdoor air based on the exhaust outlet air temperature T_{eo}. When using an

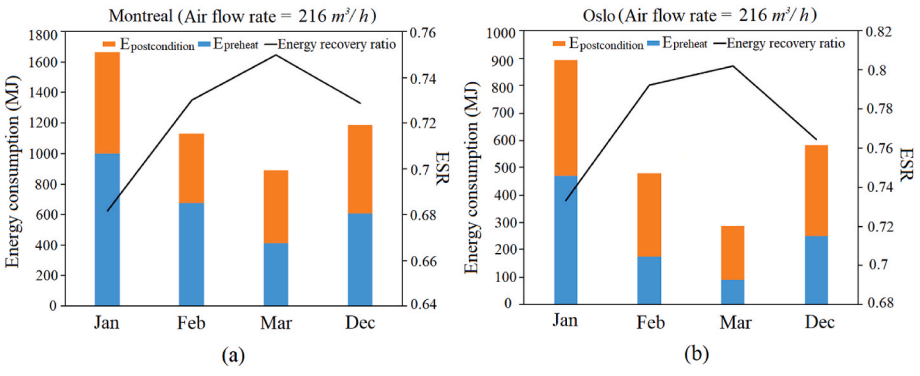

Fig. 12. Energy consumption and ESR for Montreal (a) and Oslo (b) when using the preheating outdoor air strategy during the heating season.

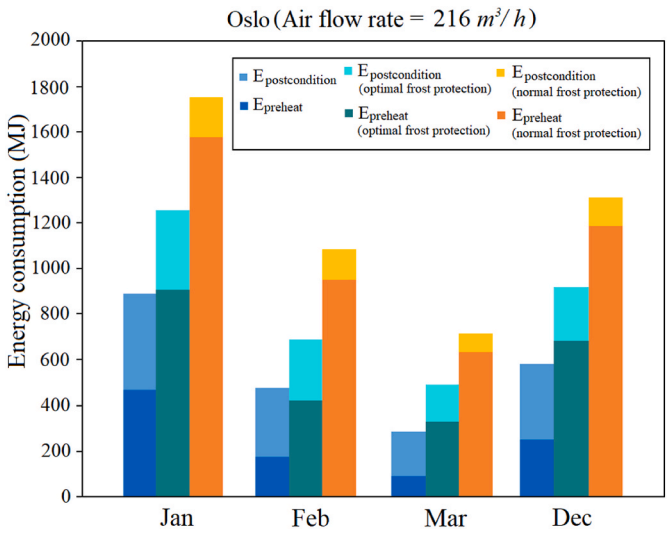

Fig. 13. Comparison between the proposed preheating outdoor air strategy, optimal frost protection and normal protection explained in the Norwegian Standard [36] for Oslo during the heating season.

enthalpy-type plate heat exchanger as the heat recovery unit, two different frost protections are defined. For optimal (economical) frost protection in residential buildings, the outdoor air temperature T_o must be heated to ensure that T_{eo} is higher than a fixed temperature of 5 °*C*. For normal (conservative) frost protection in residential buildings, T_o should be heated to ensure that T_{eo} is higher than 9 °*C*. Fig. 13 shows comparisons between the preheating outdoor air strategy as developed by the authors and the two frost protections given in the Norwegian Standard.

First, the energy consumption for pre-heating and post-heating is reduced after performing optimally. The total energy uses when using optimal frost protection method are reduced by 526.4 MJ, 403.9 MJ, 241.2 MJ and 382.8 MJ in January, February, March and December respectively compared with using normal frost protection method. The reduced energy uses account for 30%, 37.2%, 33.7%, and 29.1% of total energy use when using normal frost protection method. According to Fig. 13, the $E_{preheat}$ of using the optimal frost protection is approximately twice that of using the developed preheating outdoor air strategy. This is because when the T_{eo} must be at least 5 °*C*, as required by optimal frost protection, the outdoor air must be heated to 1 °*C*, which is higher than the threshold values in most simulated hours. For normal frost protection, the outdoor air must be heated to at least 6 °*C*. Consequently, the $E_{preheat}$ is about four times as high as that of using the developed preheating outdoor air strategy. Because the outdoor air is heated to a higher temperature when using either the optimal frost protection or normal frost protection method, the $E_{postcondition}$ values of using these methods are slightly lower than that of using the developed preheating outdoor air strategy. Concerning the $E_{tot,HR}$, using the preheating outdoor air strategy can reduce the $E_{tot,HR}$ by 32% and 54% compared with using optimal and normal frost protection, respectively.

Fig. 14 shows the energy consumption and ESR of using the heating room air strategy for Oslo in a typical week (the first week of the reference year used for simulation). $E_{tot,HR}$ consists of E_{heat} and $E_{postcondition}$ when using this strategy. Fig. 14 shows that $E_{postcondition}$ is below zero for all simulated days. This is because in order to prevent frost from developing, the room air temperature T_r needs to be heated to a significantly high temperature T_{ei}. For example, on the first day of the simulated week, the average T_{ei} required to avoid frost is 170 °*C*. In consequence, the outdoor air is overheated in the QCFMEE. In other words, T_{so} is higher than the pre-set supply air temperature T_s, which is 19 °*C*. This being the case, the postcondition process is then sensible cooling of T_{so} to T_s, which is much more difficult to achieve in reality compared with sensible heating. Fig. 14 also shows that ESR is below zero for all simulated days, indicating that using heat recovery with the heating room air strategy consumes even higher energy than ventilation without any heat recovery.

Fig. 15 illustrates the energy consumption and ESR of using the bypassing outdoor air strategy for Oslo during the heating season. In contrast to the heating room air strategy, the ESR of the bypassing outdoor air strategy remains above zero during the entire heating season. ESR is negatively impacted by $E_{postcondition}$, and the highest ESR of 0.67 occurs in the warmest month in the heating season (March), when the $E_{postcondition}$ has the lowest value of 477 MJ. The comparison of energy consumption between using the preheating outdoor air strategy and the bypassing outdoor air strategy is given in Fig. 16. It is clear that the preheating outdoor air strategy has the advantage of consuming less energy; indeed, the bypassing outdoor air strategy can use up to 2.8 times more energy than the preheating outdoor air strategy in January. For the entire heating season, preheating outdoor air uses approximately 56% less energy than bypassing outdoor air. Fig. 17 depicts the bypassed ratio $E_{bypassed}$ for the entire heating season, which fluctuates significantly between 0.24 and 0.73. This fluctuation increases the complexity of

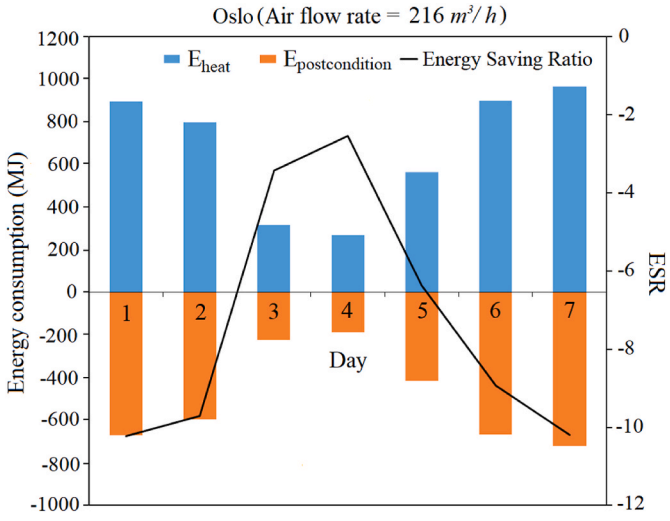

Fig. 14. Energy consumption and ESR of using the heating room air strategy for Oslo in a typical week.

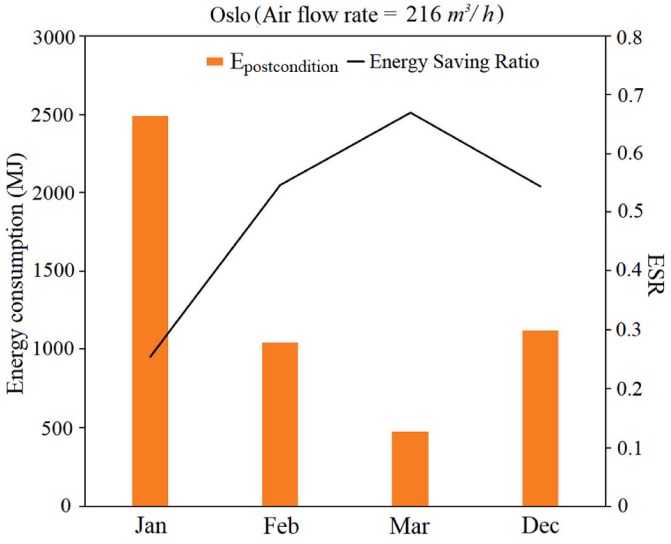

Fig. 15. Energy consumption and ESR of using the bypassing outdoor air strategy for Oslo during the heating season.

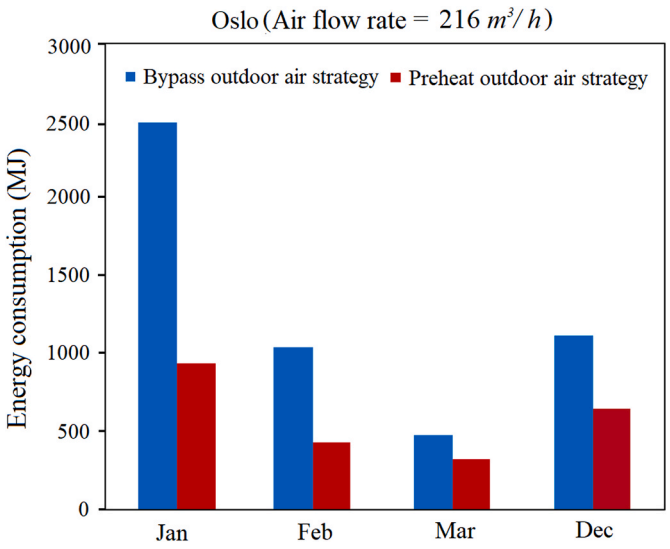

Fig. 16. Comparison of energy consumption between using the preheating outdoor air and bypassing outdoor air strategies for Oslo during the heating season.

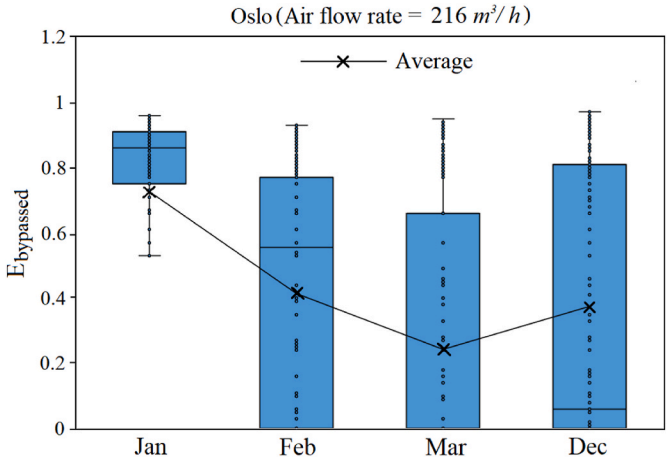

Fig. 17. Bypassed ratio $E_{bypassed}$ with the bypassing outdoor air strategy for Oslo during the heating season.

control for real-life applications.

6. Conclusions

In this paper, numerical models of QCFMEE and QCFHE were developed and validated by experimental tests. Three types of frost prevention strategies were introduced: preheating outdoor air, heating room air, and bypassing outdoor air. Their threshold values were obtained using the developed numerical models. These strategies were compared based on various criteria such as energy consumption, ESR, feasibility and complexity of control. The main conclusions are given below:

- In QCFHE, frost first occurs at the exhaust air outlet closest to the supply air inlet, which was known as the 'cold corner'. On the contrary, the frost first builds from the inside in QCFMEE rather than the 'cold corner' under all conditions because of simultaneous heat and mass transfer.
- The threshold values of the three frost control strategies are affected by several parameters: T_o, RH_r, $\dot{V}_a$ and exchanger type. Compared with QCFHE, QCFMEE has lower threshold values and thus better frost tolerance ability due to mass transfer.
- Climate has a considerable impact on the energy consumption of frost prevention strategies. In regions with cold climates, cities with an oceanic climate such as Oslo consume less energy than cities with a warm-summer humid continental climate such as Montreal. Among the discussed frost prevention strategies, the preheating outdoor strategy has the advantage of the lowest energy consumption during the heating season, and its ESR can be as high as 0.8 in Oslo. Indeed, the preheating outdoor air strategy can reduce the total energy used for ventilation with heat recovery and frost prevention $E_{tot,HR}$ by 32% and 54%, respectively, compared with the optimal and normal frost protections explained in the Norwegian Standard. The heating room air strategy consumes the most energy and faces the problem of overheating outdoor air. While the ESR of the bypassing outdoor air strategy can reach 0.67, the significant fluctuation of $E_{bypassed}$ increases the complexity of control for real-life applications.

CRediT authorship contribution statement

Hongyu Bai: Writing – original draft, Visualization, Validation, Software, Methodology, Investigation, Formal analysis, Data curation. **Peng Liu:** Writing – review & editing, Writing – original draft, Visualization, Validation, Methodology, Investigation, Conceptualization. **Hans Martin Mathisen:** Writing – review & editing, Methodology, Conceptualization.

Declaration of competing interest

The authors declare that they have no known competing financial interests or personal relationships that could have appeared to influence the work reported in this paper.

Data availability

No data was used for the research described in the article.

Acknowledgement

This study is a part of the Defreeze MEE Now project (grant number 296489), which is financially supported by the Research Council of Norway and Flexit AS, and it is a close collaboration between Flexit AS, Norwegian University of Science and Technology (NTNU) and SINTEF Community. The authors acknowledge Ms. Anneli Halfvardsson, and Dr. Fredrik Karlsson from Flexit AS for their broad experience and support.

Appendix A. Correlations of heat and mass transfer coefficients

In Eqs. (9) and (14), h_s, h_e, k_s and k_e are required for the solution of governing equations. In this study h_s is assumed to be equal to h_e and k_s is assumed to be equal to k_e. Convective heat transfer coefficient h can be obtained from Nusselt number Nu:

$$Nu = \frac{hD_H}{\lambda_a} \quad [A.1]$$

Where D_H is the hydraulic diameter of air channel (m); λ_a is the air thermal conductivity (W/mK).

Nu is obtained using Chilton-Colburn analogy, where Colburn j-factor is defined as [30]:

$$j = 0.23Re^{-0.45} \quad [A.2]$$

Where *Re* is Reynold number of air flow.

Nu is calculated based on the Chilton-Colburn analogy:

$$j = \frac{Nu}{Re\ Pr^{1/3}} \quad [A.3]$$

Where *Pr* is Prandtl number of air which is considered as a constant of 0.71.

Convective mass transfer coefficient *k* can be obtained from Sherwood number *Sh*:

$$Sh = \frac{kD_H}{D_a} \quad [A.4]$$

Where D_a is the diffusivity of air (m^2/s).

Sh is calculated using a relationship based on the Chilton-Colburn analogy:

$$Sh = NuLe^{-1/3} \quad [A.5]$$

Where *Le* is the Lewis number of air:

$$Le = \frac{Pr}{Sc} \quad [A.6]$$

Where *Sc* is Schmidt number of air which can be calculated as:

$$Sc = \frac{v_a}{D_a} \quad [A.7]$$

Where v_a is kinematic viscosity of air (m^2/s).

Appendix B. Procedures to solve governing equations

Procedures to solve governing equations are provided in this section.

The first step is to assign the boundary conditions for stream function and heat and mass transfer governing equations. For the stream function, at the inlet and the outlet of supply air channel and exhaust air channel, uniform velocity is assumed. Therefore, Neumann boundary conditions can be defined:

On supply air side

$$\frac{\partial \psi_s}{\partial y}(x = d_i + d_0, d_0 \le y \le d_i + d_0) = u_s = -\frac{\dot{m}_a}{\rho_a d_i d_a} \quad [B.1]$$

$$\frac{\partial \psi_s}{\partial y}(x = 0, 0 \le y \le d_i) = u_s = -\frac{\dot{m}_a}{\rho_a d_i d_a} \quad [B.2]$$

On exhaust air side

$$\frac{\partial \psi_e}{\partial x}(0 \le x \le d_i, y = 0) = -v_e = -\frac{\dot{m}_a}{\rho_a d_i d_a} \quad [B.3]$$

$$\frac{\partial \psi_e}{\partial x}(d_0 \le x \le d_i + d_0, y = d_i + d_0) = -v_e = -\frac{\dot{m}_a}{\rho_a d_i d_a} \quad [B.4]$$

Where geometrical properties such as d_i and d_0 of QCFMEE are defined and given in Fig. 2.

Along the geometric boundaries of QCFMEE, there is no air velocity relative to the boundaries. This means each solid boundary of QCFMEE represents a streamline. Therefore, Dirichlet boundary conditions can be defined:

On supply air side

$$\psi_s(d_0 \le x \le d_i + d_0, y = d_i + d_0) = Const \quad [B.5]$$

$$\psi_s(0 \le x \le d_o, y = x + d_i) = Const \quad [B.6]$$

$$\psi_s(d_i \le x \le d_i + d_o, y = x - d_i) = Const \quad [B.7]$$

$$\psi_s(0 \le x \le d_i, y = 0) = Const \quad [B.8]$$

On exhaust air side

$$\psi_e(x=0, 0\le y\le d_i) = Const \quad [B.9]$$

$$\psi_e(0\le x\le d_o, y=x+d_i) = Const \quad [B.10]$$

$$\psi_e(d_i\le x\le d_i+d_o, y=x-d_i) = Const \quad [B.11]$$

$$\psi_e(x=d_i+d_o, d_o\le y\le d_i+d_o) = Const \quad [B.12]$$

For heat and mass transfer governing equations, it is assumed that the temperature and humidity ratio at the inlet of supply and exhaust air channels are uniform. Dirichlet boundary conditions are defined:

On supply air side

$$T_s(x=d_i+d_0, d_0\le y\le d_i+d_0) = T_{si} \quad [B.13]$$

$$W_s(x=d_i+d_0, d_0\le y\le d_i+d_0) = W_{si} \quad [B.14]$$

On exhaust air side

$$T_e(0\le x\le d_i, y=0) = T_{ei} \quad [B.15]$$

$$W_e(0\le x\le d_i, y=0) = W_{ei} \quad [B.16]$$

All boundary conditions applied for the simulation of OCFMEE are summarized in. Fig.B.1.

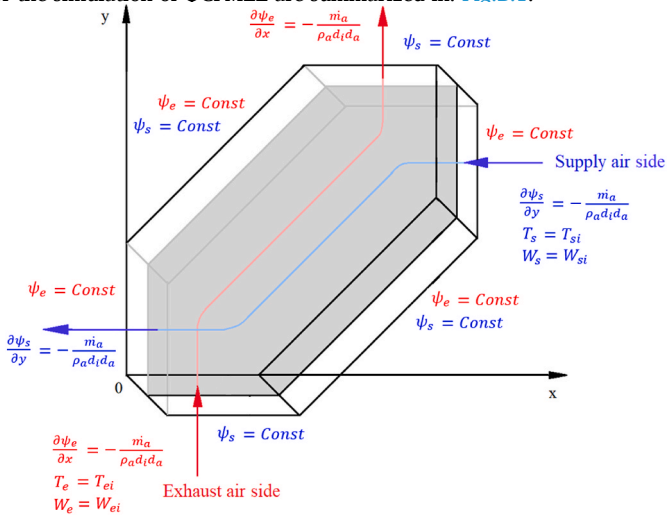

Fig. B.1. Boundary conditions applied for the simulation of QCFMEE.

Finite difference method with backward scheme is used to solve governing equations. Second-order Laplace equation (stream function) is discretized by second-order central difference scheme while heat and mass transfer equations are discretized by first-order forward difference scheme. Discretized governing equations are given below:

$$\psi_{(i,j)} = \frac{1}{4}\left(\psi_{(i+1,j)} + \psi_{(i-1,j)} + \psi_{(i,j+1)} + \psi_{(i,j-1)}\right) \quad [B.17]$$

$$T_{s(i,j)} = \frac{\frac{u_{s(i,j)}}{dx}T_{s(i,j+1)} + \frac{v_{s(i,j)}}{dy}T_{s(i-1,j)} + \frac{U}{\rho_a d_a c_{p,a}}T_{e(i,j)}}{\frac{u_{s(i,j)}}{dx} + \frac{v_{s(i,j)}}{dy} + \frac{U}{\rho_a d_a c_{p,a}}} \quad [B.18]$$

$$T_{e(i,j)} = \frac{\frac{u_{e(i,j)}}{dx}T_{e(i,j-1)} + \frac{v_{e(i,j)}}{dy}T_{e(i+1,j)} + \frac{U}{\rho_a d_a c_{p,a}}T_{s(i,j)}}{\frac{u_{e(i,j)}}{dx} + \frac{v_{e(i,j)}}{dy} + \frac{U}{\rho_a d_a c_{p,a}}} \quad [B.19]$$

$$W_{s(i,j)} = \frac{\frac{u_{s(i,j)}}{dx}W_{s(i,j+1)} + \frac{v_{s(i,j)}}{dy}W_{s(i-1,j)} + \frac{U_m}{\rho_a d_a}W_{e(i,j)}}{\frac{u_{s(i,j)}}{dx} + \frac{v_{s(i,j)}}{dy} + \frac{U_m}{\rho_a d_a}} \quad [B.20]$$

$$W_{e(i,j)} = \frac{\frac{u_{s(i,j)}}{dx}W_{e(i,j+1)} + \frac{v_{s(i,j)}}{dy}W_{e(i-1,j)} + \frac{U_m}{\rho_a d_a}W_{s(i,j)}}{\frac{u_{s(i,j)}}{dx} + \frac{v_{s(i,j)}}{dy} + \frac{U_m}{\rho_a d_a}} \quad [B.21]$$

Where i is the number of node in x direction and j is the number of node in y direction. Discretized governing equations and their corresponding boundary conditions are solved in Matlab iteratively until converged.

References

[1] L. Pérez-Lombard, J. Ortiz, C. Pout, A review on buildings energy consumption information, Energy Build. 40 (3) (2008) 394–398.
[2] C. Zeng, S. Liu, A. Shukla, A review on the air-to-air heat and mass exchanger technologies for building applications, Renew. Sustain. Energy Rev. 75 (2017) 753–774.
[3] N. Li, X. Yan, Numerical evaluation of the effects of asymmetric membrane heat conductivity and moisture adsorption hysteresis on the performance of air-to-air membrane enthalpy exchanger, Therm. Sci. Eng. Prog. (2021), 101058.
[4] L.Z. Zhang, Progress on heat and moisture recovery with membranes: from fundamentals to engineering applications, Energy Convers. Manag. 63 (2012) 173–195.
[5] A.K. Albdoor, Z. Ma, F. Al-Ghazzawi, M. Arıcı, Study on recent progress and advances in air-to-air membrane enthalpy exchangers: materials selection, performance improvement, design optimisation and effects of operating conditions, Renew. Sustain. Energy Rev. 156 (2022), 111941.
[6] J. Li, S. Shao, Z. Wang, G. Xie, Q. Wang, Z. Xu, L. Han, X. Gou, A review of air-to-air membrane energy recovery technology for building ventilation, Energy Build. 265 (2022), 112097.
[7] H.Y. Bai, P. Liu, M. Justo Alonso, H.M. Mathisen, A review of heat recovery technologies and their frost control for residential building ventilation in cold climate regions, Renew. Sustain. Energy Rev. 162 (2022), 112417.
[8] M. Justo Alonso, P. Liu, H.M. Mathisen, G. Ge, C.J. Simonson, Review of heat/energy recovery exchangers for use in ZEBs in cold climate countries, Build. Environ. 84 (2015) 228–237.
[9] P. Liu, H.M. Mathisen, M. Justo Alonso, A. Halfvardsson, C.J. Simonson, Understanding the role of moisture recovery in indoor humidity: an analytical study for a Norwegian single-family house during heating season, Build. Environ. 229 (2023) 109940.
[10] P. Liu, H.M. Mathisen, M. Skaten, M. Justo Alonso, Use of membrane energy exchanger in ventilation: odour sensory measurement, Build. Environ. 222 (2022), 109430.
[11] W. Fisk, R. Chant, K. Archer, D. Hekmat, F. Offermann, B. Pedersen, Onset of Freezing in Residential Air-To-Air Heat Exchangers, 1984.
[12] W. Fisk, K. Archer, R. Chant, D. Hekmat, F. Offermann, B. Pedersen, Performance of Residential Air-To-Air Heat Exchangers during Operation with Freezing and Periodic Defrosts, 1984.
[13] M. Rafati Nasr, M. Fauchoux, R.W. Besant, C.J. Simonson, A review of frosting in air-to-air energy exchangers, Renew. Sustain. Energy Rev. 30 (2014) 538–554.
[14] J. Zhang, A.S. Fung, Experimental study and analysis of an energy recovery ventilator and the impacts of defrost cycle, Energy Build. 87 (2015) 265–271.
[15] S. Niroomand, M.T. Fauchoux, C.J. Simonson, The mechanisms of frost formation on a semipermeable membrane, Int. J. Heat Mass Tran. 182 (2022), 121912.
[16] P. Navid, S. Niroomand, C.J. Simonson, A new approach to delay or prevent frost formation in membranes, J. Heat Tran. (2018) 141.
[17] E.G. Phillips, R. Chant, L. Bradley, D. Fisher, A model to compare freezing control strategies for residential air-to-air heat recovery ventilators, Build. Eng. 95 (1989) 475–483.
[18] P. Liu, M. Justo Alonso, H.M. Mathisen, C.J. Simonson, Energy transfer and energy saving potentials of air-to-air membrane energy exchanger for ventilation in cold climates, Energy Build. 135 (2017) 95–108.
[19] 2013 ASHRAE Handbook : Fundamentals, ASHRAE, Atlanta, GA, 2013.
[20] B. Nourozi, Q. Wang, A. Ploskić, Energy and defrosting contributions of preheating cold supply air in buildings with balanced ventilation, Appl. Therm. Eng. 146 (2019) 180–189.
[21] M. Rafati Nasr, M. Kassai, G. Ge, C.J. Simonson, Evaluation of defrosting methods for air-to-air heat/energy exchangers on energy consumption of ventilation, Appl. Energy 151 (2015) 32–40.
[22] A. Pacak, A. Jedlikowski, D. Pandelidis, S. Anisimov, Analysis of freeze protection methods for recuperators used in energy recovery from exhaust air, E3S Web of Conferences 22 (2017), 00129.
[23] X. Luo, W. Roetzel, Theoretical investigation on cross-flow heat exchangers with axial dispersion in one fluid, Rev. Gen. Therm. 37 (3) (1998) 223–233.
[24] W.J. Fisk, R.E. Chant, K.M. Archer, D. Hekmat, F.J. Offermann Iii, B.S. Pedersen, Onset of freezing in residential air-to-air heat exchangers, Build. Eng. (1985).
[25] J.M. Robertson, Hydrodynamics in Theory and Application, Prentice-Hall, 1965.
[26] M. Rafati Nasr, F. Fathieh, D. Kadylak, R. Huizing, R.W. Besant, C.J. Simonson, Experimental methods for detecting frosting in cross-flow air-to-air energy exchangers, Exp. Therm. Fluid Sci. 77 (2016) 100–115.
[27] P. Liu, M. Rafati Nasr, G. Ge, M. Justo Alonso, H.M. Mathisen, F. Fathieh, C. J. Simonson, A theoretical model to predict frosting limits in cross-flow air-to-air flat plate heat/energy exchangers, Energy Build. 110 (2016) 404–414.
[28] P. Liu, H.M. Mathisen, M. Justo Alonso, C.J. Simonson, A frosting limit model of air-to-air quasi-counter-flow membrane energy exchanger for use in cold climates, Appl. Therm. Eng. 111 (2017) 776–785.
[29] ASHRAE, Standard 55-2020 Thermal Environmental Conditions for Human Occupancy, 2020. Atlanta, GA.
[30] P. Liu, M. Justo Alonso, H.M. Mathisen, C.J Simonson, Performance of a quasi-counter-flow air-to-air membrane energy exchanger in cold climates, Energy Build. 119 (2016) 129–142.
[31] H.W. Coleman, W.G. Steele, Experimentation and Uncertainty Analysis for Engineers, second ed. ed, John Wiley & Sons, New York, 1999.
[32] W.M. Kays, A.L. London, Compact Heat Exchangers, United States: McGraw-Hill, New York, NY, 1984. Medium: X; Size: Pages: 3352008-02-07 McGraw Hill Book Co., 1221 Avenue of the Americas, New York, NY 10020.
[33] M. Kottek, J. Grieser, C. Beck, B. Rudolf, F. Rubel, World map of the Köppen-Geiger climate classification updated, Meteorol. Z. 15 (3) (2006) 259–263.
[34] Heating degree days (18°C) - annual data for montréal. https://montreal.weatherstats.ca/charts/hdd-yearly.html.
[35] https://energy-data.io/energy-tools/degree-day-calculator-free/.
[36] SN-NSPEK 3031:2021, Energy Performance of Buildings — Calculation of Energy Needs and Energy Supply, 2021. Oslo.